Urban surface temperature observations from ground-based thermography: intra- and inter-facet variability

Urban surface temperature observations from ground-based thermography: intra- and inter-facet variability

William Morrison[a], Simone Kotthaus[a,b], Sue Grimmond[a]

[a]Department of Meteorology, University of Reading, Earley Gate, Reading, RG6 6BB, UK
[b]Institut Pierre Simon Laplace (IPSL), École Polytechnique, CNRS, Université Paris-Saclay, 91128 Palaiseau Cedex, France

Abstract

Ground based thermal cameras are used to observe urban surface temperatures (T_s) with an unprecedented combination of: temporal and spatial resolution (5 min and ~0.5 m → 2.5 m), spatial extent (3.9 ha), instrument number (6 static cameras) and surface heterogeneity (mixed high rise and vegetation). Unsupervised classification of images by geometry and material properties (surface orientation, albedo, solar irradiance, and shadow history) is facilitated by a detailed three-dimensional surface model (430 m x 430 m extent) and sensor view modelling. From detailed source area analysis, 9.5 % of the area is observed by the cameras. Across all camera pixels, the 5th - 95th percentile T_s differences reach 37.5 K around midday. Roofs have the greatest diurnal T_s range (290.6 K → 329.0 K). T_s differences across sunlit sloped roofs reach 23.3 K. Walls of different cardinal orientations consistently differ by > 10 K between 10:00 and 15:00. Shadow tracking within images is used to model cooling rates, where recently shaded (< 30 min) ground can be 18.6 K warmer than equivalent unshaded T_s. West walls remain warm past sunset and are 1.2 K warmer than north walls at 23:00 (~4 hours after sunset). Recently shaded walls cool exponentially to ambient T_s at a similar rate as the ground, but four times slower than roofs. The observed T_s characteristics are anticipated to have a wide range of applications (e.g. evaluation of urban surface energy balance models, ground-truthing of satellite thermal remote sensing).

1. Introduction

Urban surface temperature (T_s) is an important control in the surface energy balance (Krayenhoff and Voogt, 2007) that has distinct characteristics across cities (Offerle *et al.*, 2006). There is increasing interest in T_s observations with high temporal and spatial resolution at facet (e.g. roof, wall, ground) and sub-facet (e.g. materials, shadowing) scales as the degree of urban modelling complexity required for atmospheric models is unclear (Chen *et al.*, 2011). Numerical weather prediction (NWP) frequently characterises the urban surface energy balance by facet (e.g. TEB, Masson, 2000; MORUSES, Porson *et al.*, 2010; SLUCM, Kusaka and Kimura, 2004; BEP, Krayenhoff *et al.*, 2020). Increasingly complex and realistic sub-facet details within urban areas are resolved by models for: computational fluid dynamics (CFD) (Toparlar *et al.*, 2017), sub-facet surface energy balance (e.g. TUF3D, Krayenhoff and Voogt, 2007; THERMORender, Xu and Asawa, 2020), thermal radiation stress (e.g. SOLWEIG, Lindberg and Grimmond, 2011; RayMan, Fröhlich *et al.*, 2019) and building

energy (e.g. EnergyPlus, Crawley *et al.*, 2001). Such models may have T_s as a prognostic variable which requires observational evaluation across the facets resolved by the model processes.

High temporal and facet-scale resolution urban T_s observation for model evaluation faces many challenges resulting in a general lack of such studies (Toparlar *et al.*, 2017). Exploiting space-borne data for evaluation (e.g. Alexander *et al.*, 2015 using MODIS; Toparlar *et al.*, 2015 using Landsat) is constrained by: low revisit times, a view bias of horizontal surfaces (Hu and Wendel, 2019), and low spatial resolutions such that one pixel may cover the entire model domain (e.g. MODIS, Meteosat Second Generation). Thermal cameras on airborne platforms (e.g. helicopters Hénon *et al.*, 2012; Antoniou *et al.*, 2019; drones Gaitani *et al.*, 2017; Naughton and McDonald, 2019) can view the convoluted urban surface at facet-scale but also have low revisit times and directional view bias (Lagouarde *et al.*, 2004). These studies typically assume no atmospheric effects (Meier *et al.*, 2011; Morrison *et al.*, 2020) on observations. From ground-based platforms, thermal cameras have potential to supersede point-based *in-situ* sensors (e.g. thermocouples used by e.g. Kanda *et al.*, 2005; Rotach *et al.*, 2005; Pearlmutter *et al.*, 2006) due to higher temporal and spatial resolutions to observe both inter- and intra- facet variations (e.g. Alchapar *et al.*, 2014). A few studies (e.g. low-rise suburb, Adderley *et al.*, 2015; scale model, Morrison *et al.*, 2018) achieve adequate spatial coverage but are limited to simple surface heterogeneity. Ground- or airborne sub-facet thermal imagery across more realistic cities is rare, given the challenges with: logistics to obtain adequate camera views of the convoluted three-dimensional surface and classifying the observations to know what is actually sampled and therefore can/should be compared to model outputs. Sub-facet resolution sampling is done on foot at street level (e.g. Lee *et al.*, 2018) or with vehicle traverses to sample more walls and ground (e.g. Voogt and Oke, 1997; Hilland and Voogt, 2020). Other thermography observations have increased spatial coverage using Asano and Hoyano's (1998) spherical sampling technique (e.g. Acuña Paz y Miño *et al.*, 2020), rotating masts (Adderley *et al.*, 2015), or multiple cameras (e.g. Morrison *et al.*, 2020). Classification methods have used time consuming and subjective techniques such as manual digitisation (Hartz *et al.*, 2006; Lee *et al.*, 2018; Antoniou *et al.*, 2019) or supervised clustering (Voogt and Oke, 1997; Hénon *et al.*, 2012). To expand classification possibilities, Hilland and Voogt (2020) use concurrent visible imagery.

The objectives of this paper are to: (i) outline an unsupervised and objective method to analyse surface-based thermal remote sensing images and (ii) investigate the drivers of urban T_s variability at a high level of detail. The Morrison *et al.* (2020) London network of six ground-based infrared cameras is used to obtain unprecedented T_s detail (5 min temporal and ~ 1 m spatial resolution) for a local-scale area, giving unique insight into urban T_s variability. A digital surface model (DSM) is used with perspective projection and radiative transfer modelling to objectively classify observations by transient sun-surface geometry effects that would not be possible by manual or supervised means.

2. Methods

To investigate the drivers of urban T_s variability, ground-based thermal camera observations are processed to determine the surfaces "seen" across a range of scales, from building scale features (facet, orientation and bulk material) through to sun-surface geometry and shadow history at the sub-facet scale.

2.1. Study area and observations

Observation sites in the Borough of Islington, London, UK (51°31'35" N, 0°06'19" W) on two high rise residential tower blocks are identified (ID) as "IMU" and "WCT" (IMU at 74 m agl (above ground level); WCT 36 m agl) (Fig 1a). The study area covers a real world (RW) area with irregular street pattern with streets often lined with deciduous trees. There is a mix of residential and commercial buildings (often four to six storeys tall) arranged in terrace rows or large single units (Fig 1d).

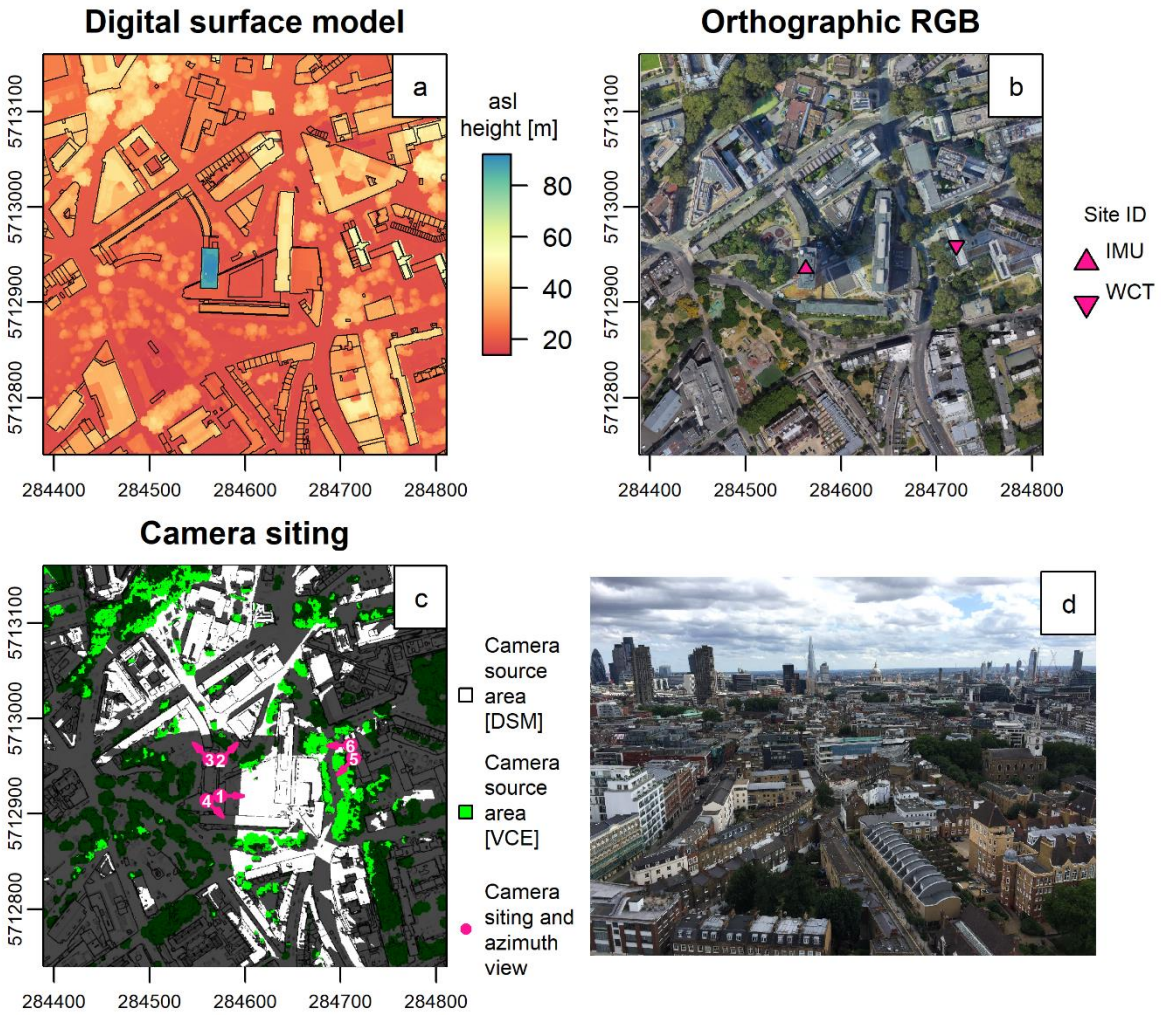

Fig 1. Plan view of study area with: (a) height of all surfaces above sea level (asl) with building footprints (black lines, from Evans *et al.*, 2011), (b) orthorectified RGB image from a mosaic of Google Earth (Google, 2019) images with locations (symbols) of the study sites, (c) a render of the "model world" (MW) digital surface model (DSM) and vegetation canopy element (VCE) geometry with DSM (white) and VCE (green) seen by the cameras located (pink dots) around the observation sites with different view directions (pink arrows) and unique camera identification (white) numbers (Table 1 gives details), (d) Digital camera image looking southeast and next to camera number 4 (C4) on 25th Oct 2017. (a – c) use Coordinate Reference System WGS84 UTM grid zone 31N. (a-c) are modified from Morrison *et al.* (2020).

Optris PI-160 (Optris GmbH, 2018) longwave infrared (LWIR) cameras (Table 1) measure upwelling longwave radiation from the study area (Fig 1c) for 27th – 28th August 2017 (mainly clear-sky summer days). The cameras have multiple view angles (Table 2) allowing various facets of the complete canopy surface to be sampled. Morrison *et al.* (2020) provide details on the study area and the observations, including: camera siting, measurement procedure, meteorological conditions, and the atmospheric and emissivity corrections of observations to estimate T_s from the at-sensor brightness temperatures. Downwelling shortwave (SW) irradiance ($E_{SW}^{\downarrow}$, W m^{-2}) from a Davis Vantage Pro 2 weather station located 114 m agl, 1.1 km southeast of IMU aids the image classification.

Table 1. Measurement and corrections used to determine surface temperature (T_s) from longwave infrared (LWIR) cameras.

Property	Description
Platform	Static ground-based
Sample rate	1 min
Temporal resolution	5 min (median of samples at end of interval)
Image resolution	160 x 120 pixels
Temperature resolution	0.1 K
Number of cameras	6
Observation campaign period	7th July – 10th Nov 2017 (here 27th – 28th August)
Enclosure	Custom built enclosures (Morrison *et al.*, 2020)
Radiometric calibration	Manufacturer calibrated 2 months prior to study
Accuracy	± 2 K
Spectral range	7 – 14 µm, see Morrison *et al.* (2020)
Image distortion correction	Rectilinear correction; see Morrison *et al.* (2018)
Atmosphere correction	Multi line of sight; see Morrison *et al.* (2020)
Emissivity correction	Corrected for multiple scattering with anisothermal surface emission; see Morrison *et al.* (2020)

Table 2. Siting properties of the ground based LWIR cameras installed on two high-rise residential towers named "IMU" and "WCT" within the study area (Fig 1).

Camera ID	Location Site ID	Field of View (°) horizontal x vertical	Cardinal Facing	Viewing Zenith Angle (Θ, °)	Median Path Length (m)
C1	IMU	68.6 x 54.2	E	46.5	88.8
C2	IMU	62.6 x 49.1	NE	51.7	97.9
C3	IMU	62.8 x 49.2	NWW	52.9	106.6
C4	IMU	37.3 x 28.4	SE	56.7	122.7
C5	WCT	38.4 x 29.3	SW	66.6	79.0
C6	WCT	62.4 x 48.9	W	61.7	67.5

2.2. Image classification

To facilitate image classification, the RW study area and instrumentation are represented in a "model world" (MW). The MW uses a vector-based 3D DSM with a 3D mesh of triangles and a voxelated representation of vegetation covering the RW study area (Fig 1). The DSM extends 430 m x 430 m horizontally to cover the camera source areas. The MW also uses sensor view modelling to replicate the RW camera perspectives (hereafter "MW cameras"), whereby the DSM is projected on to the MW camera image plane, using a pinhole camera projection (Hartley and Zisserman, 2004).

Modelled camera perspectives determine various surface types "seen" by each camera pixel (x, y). Types of surface are differentiated by class (i) at timestep t for each pixel [i(x, y, t)]. Within class i, three surface properties are defined (Table 3): orientation and material (Σ), sun-surface geometry (bidirectional reflectance factor, BRF) and shadow history (time in shade, t_{shd}, min). Thus i principally describes sun-surface geometry which is a key driver of T_s variability (Krayenhoff and Voogt, 2016; Morrison *et al.*, 2018).

Many features of the MW are created and managed by the Discrete Anisotropic Radiative Transfer (DART) model (Gastellu-Etchegorry *et al.*, 2012). DART allows 3D radiative transfer (RT) processes to be simulated in both natural and urban landscapes in the visible to LWIR regions of the

electromagnetic spectrum using a ray tracing approach. Here DART is used to simulate the BRF "seen" by each MW camera pixel, shown by Morrison *et al.* (2018) for simple building geometry to differentiate sunlit and shaded areas. For a full description of DART see Gastellu-Etchegorry *et al.* (2015).

Orientation and material (Table 3) for each camera pixel [$\Sigma(x, y)$, Fig 2b] is obtained using Blender rendering software (Blender, 2018), where DSM triangle colours are rendered for each MW camera image perspective (Morrison *et al.*, 2018 for details). A pixel is $\Sigma_{mixed}(x, y)$ (dark grey, Fig 2b) if it (a) has more than one surface and orientation property rendered or (b) views surfaces beyond the MW extent (e.g. Fig 2b C2, top of image). Pixels manually masked [$\Sigma_{masked}(x,y)$] from further analysis include near-field IMU and WCT roofs which are challenging to align, a low emissivity metal roof (C2, Fig 2b) and the corner of the C1 enclosure (Fig 2b, top left). Compared to prior studies that manually classify images, our classification is objective and automated but typically has fewer classes. Christen *et al.*'s (2012) images classified by manual inspection and digitisation (see their Fig 1d) include e.g. brick/painted walls and tile/gravel roofs by manual inspection and digitisation. Inclusion of such classes here - in Σ and across Fig 2b - would require a similarly classified DSM which was not available in this study.

To determine the sun-surface geometry characteristics (Table 3), all MW surfaces, including vegetation canopy elements, are defined in DART as opaque Lambertian reflectors. Direct downwelling spectral irradiance ($E_\lambda^{\downarrow,dir}$, W m^{-2} μm^{-1}) is simulated by DART at 0.5 μm wavelength (λ, bandwidth $\Delta\lambda$ = 0.01 μm). Rays originate from a horizontal layer just above the tallest building (625 rays m^{-2}) and are tracked downward with spectral radiant flux density $E_\lambda(\theta, \phi, \Omega, t)$ (W m^{-2} μm^{-1}) along solid angle Ω (sr) and direction (θ, ϕ) at timestep t. $E_\lambda(\theta, \phi, \Omega, t)$ intercepted by the MW surface is scattered for all possible scattering directions, according to the surface position and orientation. Scattered rays that intercept the image plane of a MW camera are used by DART to calculate at-sensor spectral radiance [$L_\lambda^{cam}(x, y, t)$, W m^{-2} sr^{-1} μm^{-1}].

The BRF across the camera images is calculated as:

$$BRF(x, y, t) = \frac{\pi L_\lambda^{cam}(x, y, t, \Omega)}{E_\lambda^{\downarrow,dir}(t)}. \qquad \text{Eqn. 1}$$

For a shaded surface BRF is zero. BRF = 1 for sunlit horizontal surfaces (i.e. surfaces plane-parallel to the ground) regardless of daytime sun angle and camera view angle, as $E_\lambda^{\downarrow,dir}$ is referenced to a horizontal layer. The BRF of a non-flat surface departs from unity. BRF increases as the sun angle becomes perpendicular to the surface, and vice versa. For example, in the northern hemisphere, east facing walls have the highest BRF in the early morning, decreasing through the morning as the sun-surface angle becomes more oblique.

A low density of rays incident on a surface can occur if the direct-beam solar radiation is near-perpendicular to a surface and/or when the sun angle is low relative to the surface. This can cause inaccuracies and erroneous patterns in BRF(x, y) and isolated "sunlit" pixels [BRF(x, y) > 0] (i.e. none of the surrounding 8 pixels have BRF(x, y) > 0). To resolve this, in this study we reassign these pixels to $\Sigma_{mixed}(x, y)$. Where BRF(x, y, t) has a continuous scale, the final surface property for analysis is $\overline{BRF}(x, y, t)$, which is BRF(x, y, t) binned (indicated by overbar) between $0 \rightarrow 2$ using a bin width of 0.25. The bins are centre labelled. The first bin is 0 and is for values between 0 and 0.125 e.g. BRF(x, y, t) = 0.10 is assigned to $\overline{BRF}(x, y, t) = 0$; the second bin is 0.25 and has values between 0.125 and 0.375 e.g. BRF(x, y, t) = 0.13 is assigned $\overline{BRF}(x, y, t) = 0.25$; etc. To differentiate shaded pixels [BRF(x, y, t) = 0] from the lowest $\overline{BRF}$ bin ($\overline{BRF}(x, y, t) = 0$), pixels with BRF(x, y, t) < 0.05 on timesteps with no direct solar radiation are assigned to a separate bin, $\overline{BRF}(x, y, t) = -1$ for analysis. $E_{SW}^{\downarrow}$ observations (Section 2.1) are considered to have no direct solar radiation if they fall below a threshold of modelled clear-sky direct and diffuse insolation (Bird and Hulstrom, 1981, model implemented in *solaR* software, Perpiñán, 2012).

Shadow history is defined for the time a surface has spent in shade (t_{shd}, min) (Table 3) and is determined by comparison of $\overline{BRF}(x, y, t)$ to the prior timestep [$\overline{BRF}(x, y, t - 5min)$]. If a surface becomes shaded at time t, it has spent $t_{shd}(x, y, t) = 5$ min in shade. For the timestep prior to this (t - 5 min), the surface has spent zero minutes in shade and has $t_{shd}(x, y, t - 5min) = 0$ min. A surface that continues to be in shade [i.e. $\overline{BRF}(x, y, t + 5min) = -1$] has $t_{shd}(x, y, t + 5\ min) = 10$ min at the next timestep, etc. As a pixel can view a surface that is part sunlit and part shaded across multiple timesteps, these pixels are designated fully sunlit or fully shaded based on the 10-timestep (50 min) window around each timestep. If a pixel has $\overline{BRF}(x, y, t) > -1$, is sunlit at t - 25 min and shaded at t + 25 min, then it is considered partially sunlit at t. In these cases, the following threshold is used to determine if the observed surface is more shaded than sunlit and $t_{shd}(x, y, t)$ is updated accordingly:

$$t_{shd}(x,y,t) = \begin{cases} 0 & \text{if } BRF(x,y,t) < [0.75 \cdot BRF(x,y,t - 25\ min)] \\ 5 & \text{otherwise} \end{cases}. \qquad \text{Eqn. 2}$$

If $t_{shd}(x,y,t) = 0$, pixels are allocated the maximum $\overline{BRF}(x, y)$ that occurred up to 5 timesteps prior (i.e. $\max\{\overline{BRF}(x, y, t - 25\ min \rightarrow 0)\}$) to assign partially shaded pixels with a fully sunlit status.

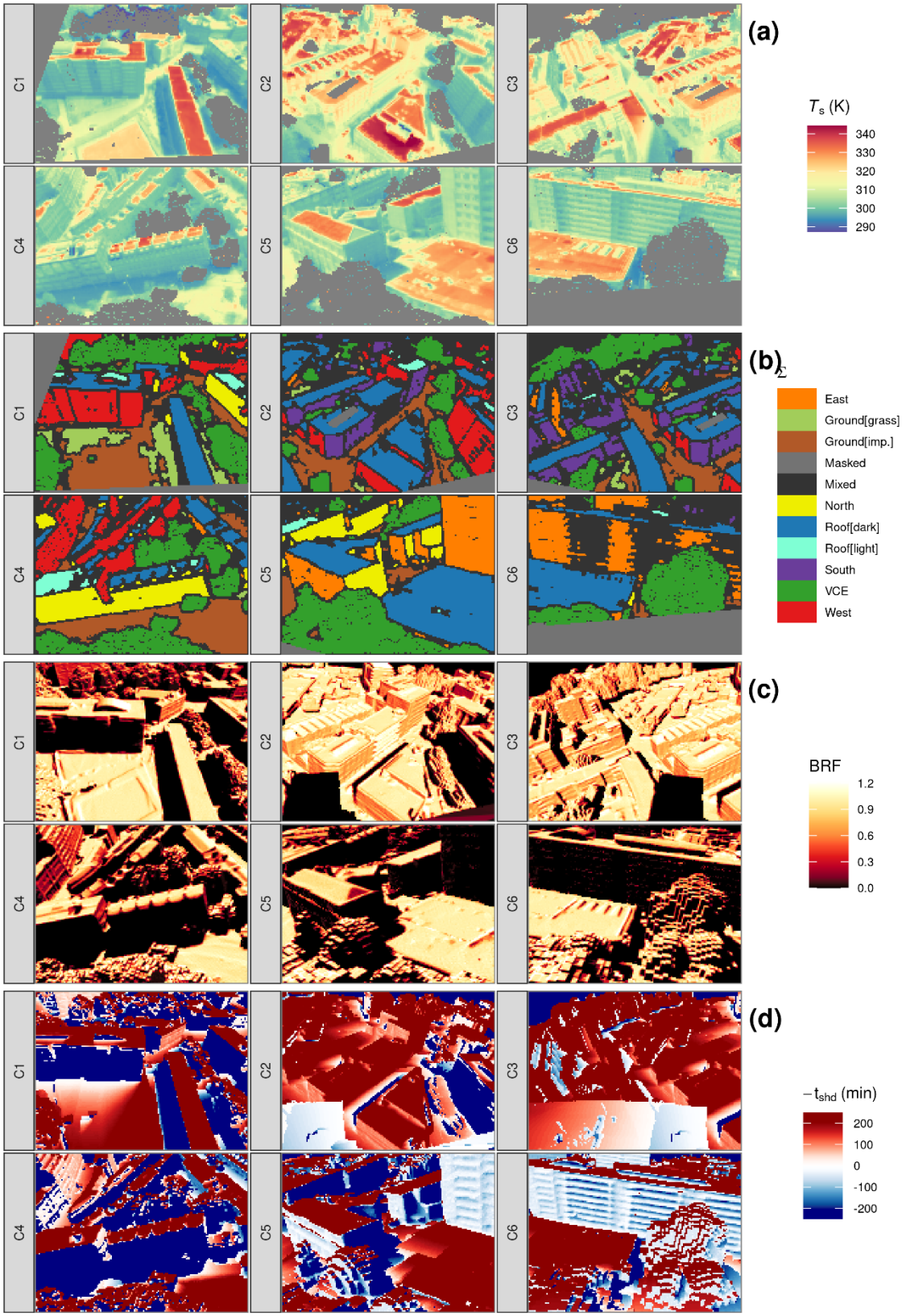

Fig 2. (a) Optris PI longwave infrared (LWIR) camera observations for 27th August 2017 12:00 UTC and (b – d) simulated surface properties projected onto the image plane of "model world" (MW) cameras that simulate the perspective of (a). Surface properties are: (b) orientation and material (Σ), (c) shortwave bidirectional reflectance factor (BRF) to determine sun-surface geometry assuming Lambertian reflecting surfaces, and (d) time surfaces have spent in shade (t_{shd}, white → blue) or sun (white → red). The cameras (Table 2) are indicated to the left of each image. (a-b) are modified from Morrison *et al.* (2020).

Table 3. Surface properties of orientation and material (Σ), bidirectional reflectance factor (BRF) and shadow history (t_{shd}) used for per-pixel classification of LWIR camera observations (Fig 2). A surface class (i) has three surface properties: Σ, $\overline{BRF}$, t_{shd}.

	Property	Method	Description	Values		Example
Σ	Orientation and material	Blender 3D modelling Land cover map Airborne hyperspectral (Morrison *et al.*, 2020)	Cardinal orientation and material	Roof[dark] Roof[light] Ground[imp.] Ground[grass] North East	South West Down Mixed Masked	Fig 2b Fig 3
$\overline{\text{BRF}}$	Sun-surface geometry	DART simulation	DART bidirectional reflectance factor (BRF) simulation	BRF binned ($\overline{\text{BRF}}$) as $0 \rightarrow 2$ at $\Delta 0.25$ (unitless). Shaded surfaces (BRF < 0.05) are assigned to bin $\overline{\text{BRF}}$ = -1		Fig 2c
t_{shd}	Shadow history	DART simulation	Time in shade	$0 \rightarrow 2\tau\ \Delta 5$ (min)		Fig 2d

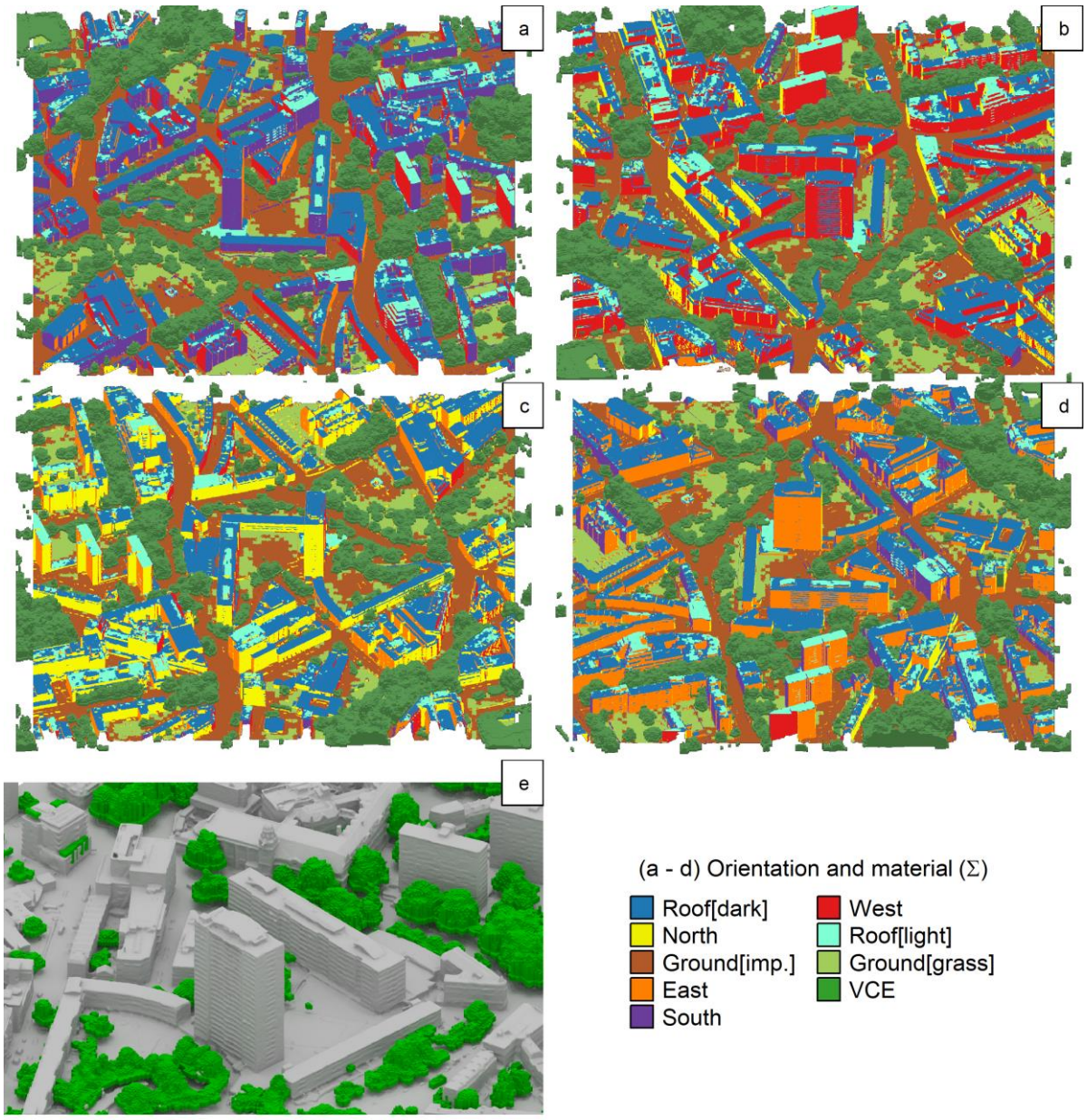

Fig 3. Vector digital surface model (DSM) and vegetation canopy elements (VCE) for the study area created from Google Earth (Google, 2019; Morrison *et al.*, 2020) imagery with (colours) orientation and material surface properties (Σ) rendered in Blender (Blender, 2018) for off-nadir view directions facing: (a) north, (b) east, (c) south, (d) west and (e) northeast with focus on the study sites and surface geometry, rendered without Σ. VCE covers a slightly larger area than the DSM.

2.3. Cooling events

A "cooling event" time window is used to analyse the shadow history (Section 2.2) effect on observed T_s. This starts when a pixel is sunlit for the last time ($t_{shd}(x, y) = 0$ min) and ends when it is substantially cooled ($t_{shd}(x, y) > n\tau$), with time constant τ (min) and multiplicative factor n. A cooling event can continue after sunset and across days. To determine a representative time window for cooling events, τ is calculated using an exponential rate of cooling (Vollmer, 2009) for all pixels that enter shade as:

$$T_s[a] = T_s[b] + (T_s[c] - T_s[d])e^{\left(-\frac{t}{\tau}\right)} \quad \text{Eqn. 3}$$

using T_s observation subsets (Table 4). In Eqn. 3, the T_s difference for recently shaded (T_s[a]) and prolonged shaded (T_s[b], hereafter "ambient" T_s) surfaces throughout the cooling event isolates the rate of cooling from any ambient variations in surface temperature. The ambient temperature is included in the cooling event definition as it isolates the direct solar irradiance component of the surface energy balance from all other energy balance processes. These include variations in sensible heat exchange (from e.g. wind speed and direction), incoming diffuse radiation (due to e.g. patchy cloud or day-night transition) and heat storage. After τ minutes, the temperature difference is reduced to 1/e (~0.368) of the value at $t_{shd} = 0$ (Vollmer and Möllmann, 2017).

Table 4. Surface temperature sub-classes used to determine exponential cooling (Eqn. 3). See text and Table 3 for definitions. Cooling event lengths (nτ) have units of minutes

	Surface temperature ($\boldsymbol{T_s}$) description	Definition
T_s[a]	Pixel T_s with time in shade no longer than nτ	$T_s(x, y, \Sigma, \overline{BRF} > -1, t_{shd} > 0 \,\&\, \leq n\tau, t)$
T_s[b]	Ambient T_s at time t, aggregated (median) from pixels in shade for more than nτ	$T_s(\Sigma, \overline{BRF} = -1, t_{shd} > n\tau, t)$
T_s[c]	Pixel T_s at the timestep prior to shadowing ($t_{shd} = 0$), i.e. at start of the cooling event (t = 0)	$T_s(x, y, \Sigma, \overline{BRF} > -1, t_{shd} = 0, t = 0)$
T_s[d]	Ambient T_s at the timestep prior to shadowing (t = 0), aggregated (median) from pixels in shade for more than nτ	$T_s(\Sigma, \overline{BRF} = -1, t_{shd} > n\tau, t = 0)$

Cooling event lengths (nτ) need to be initially estimated. Using all pixels within a day for a given surface orientation and material, nτ is set at 15 min and increased incrementally until the majority of observations are at ambient T_s; i.e. when > 68% of pixels with $t_{shd}(x, y) = n\tau$ have an exponentially cooled T_s (T_s[a]) that is lower than the ambient temperature (T_s[b], median) plus one standard deviation. Cooling events are only considered if a pixel has a temperature recorded at $t_{shd}(x, y) = 0$ and $t_{shd}(x, y) = n\tau$.

To demonstrate cooling events, $T_s(x, y)$ for recently shaded surfaces (Fig 4a, black and grey) and an aggregated value of all pixels viewing surfaces that have been shaded for an extended (>nτ) period ("ambient" temperature, Fig 4a, blue) are compared over 1.5 h (Fig 4b is one randomly selected cooling event). From this, τ(x, y, t) (Eqn. 3) is estimated using a nonlinear least squares (NLS) model fit for all per-pixel cooling events (Fig 4b, red). Across all pixels during the study date, the NLS fit of τ(x, y, t) is rejected if (1) it contains less than 5 timesteps, (2) the pixel surface property becomes "mixed" (Section 2.2) at any point during the event, (3) the NLS fit fails to converge, or (4) τ(x, y, t) > 1000 min. A generalised modelled value of τ uses the median value of τ(x, y, t, Σ) determined from all eligible cooling events across the study date as one representative time constant for three surface types: roofs, walls, and ground [τ(Σ)].

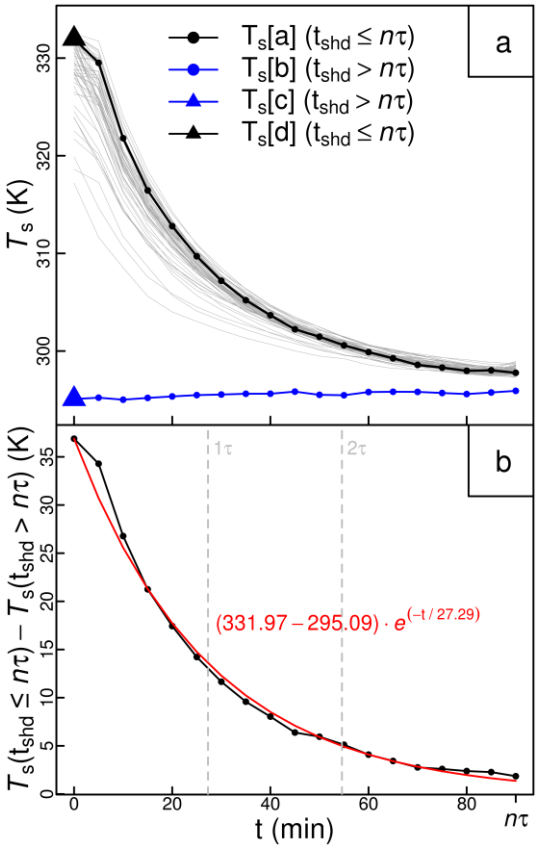

Fig 4. Visual definition and example of "cooling events". These occur after a surface becomes shaded and are parameterised by an exponential rate of cooling. Shown here for all C3 camera roof-viewing pixels shaded from t = 0 and t = 90 (min) (10:00 and 11:30 on 27th August 2017) with: (a) all samples (grey lines) and one (random, black) cooling event with the "ambient" surface temperature (blue) line) (b) modelled with an exponential fit (red, Eqn. 3) for one (black line from a) cooling event.

3. Observational source area

Of the total model world (MW) surface area (A_{TOTAL} = 4.1 x 10^5 m^2, Fig 5), 88.0 % is composed of DSM triangles and the remainder (12.0 %) is from the vegetation canopy elements (VCE) plan area. East and west walls are 23.3 % of A_{TOTAL} compared to 18.3 % for north and south walls. These numbers are not equal as the MW buildings are not cuboids and some are cut off at the MW edges (Fig 3). The ground surfaces (30.3 %) (e.g. streets, parks, courtyards) have greater area than the roofs (15.6 %). Roofs mostly have low albedo (Roof[dark], 12.8 %).

The overall camera source area (A_{CAM}) is 38,950 m^2 (9.5 % of A_{TOTAL}), approximated as the summed area of triangles completely within the field of view of any camera. A_{CAM} excludes VCE directly but resolves the occlusion of other surfaces by VCE. Where cameras have overlapping source areas (Fig 1c, Fig 2) the overlapping area is allocated arbitrarily to the camera with lowest ID (Table 2). With A_{CAM} calculated using the DSM triangles (not rendered images), it includes all mixed ("complex" geometry) and masked (near field objects, e.g. roofs directly beneath cameras, Fig 2b) pixels causing a small overestimation of A_{CAM}. A_{CAM} may further underestimate the actual source area of classified pixels, as partially visible triangles (MW camera field of view) are rejected.

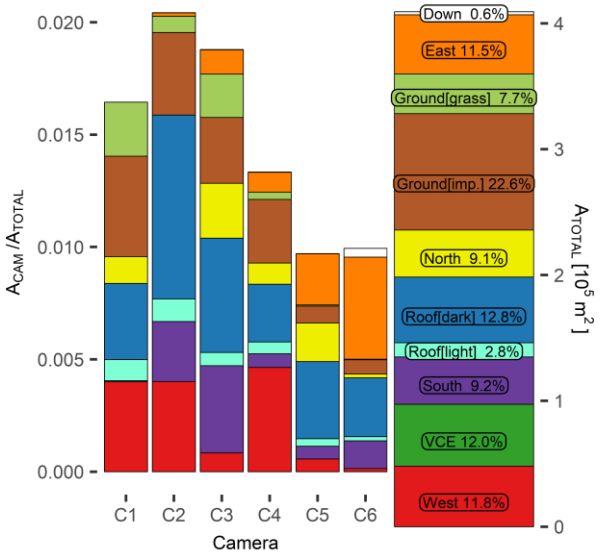

Fig 5. Total three-dimensional study surface area (A_{TOTAL}) and area seen by the LWIR cameras (A_{CAM}) (Table 2) classified by surface and orientation properties (colours).

Inter-camera differences in A_{CAM} result from camera siting height, zenith view angle and the occlusion of far-field surfaces by near-field objects. Located at 75 m agl with an oblique view angle, camera C2 has the largest source area (2 % of MW area, Fig 5) whereas C5 and C6, mounted at 37 m agl, have the smallest source areas (~ 1 % of MW each). Roof and ground surfaces are observed by all cameras. The oblique view angles mean vertical facets substantially contribute to the observational source area, but the actual vertical facets sampled depends on the camera azimuth. A camera can view surfaces with opposing directions (e.g. east and west) due to the grouping of the heterogeneous wall facings into the four cardinal directions.

For pixel-level source areas, the manual approach used to determine A_{CAM} (Fig 5) is too time consuming to conduct for each of the 1.15 x 10^5 individual pixels. Variations in surface area coverage across each camera IFOV (instantaneous field of view) are not accounted for and pixels are assumed to have equal source areas. The azimuth and zenith of DSM triangles within each camera pixel IFOV are given in Fig 6. The distribution of surface azimuth angles for the walls is uneven (Fig 6a). Some angles have many samples (maximum = 2677 pixels, for 342.5° → 347.5°) and others far fewer (minimum = 130 pixels, for 127.5° → 132.5°) as building walls have a few fixed directions and sensors have limited views (Table 2). Given the complexity of the study area geometry, the azimuthal facings are well distributed within each wall orientation bin (Fig 6a, between vertical dashed lines) except for the Σ_{South} where a view bias of southeast facing ($\theta \approx 135° \rightarrow 150°$, Fig 6a) surfaces is found. This is explained by the southwest-to-northeast street orientation sampled by the northward facing cameras (C2 and C3).

Sloped roofs, chimneys, balconies and other micro-scale geometry resolved in the DSM widen the surface zenith angle distribution (Fig 6b). The incorrect classification of highly sloped roofs as walls and the DSM "rounding" of corners over short (< 1 m) distances also contribute towards this broad

surface zenith angle distribution. Most observed walls are vertical (median 90.83°) with variability (±11.07° standard deviation) from the sub-facet wall geometry (e.g. balconies). Roof pixels are mainly flat (median 176.74°). Here, slight slopes (e.g. 8579 pixels sample roofs with surface zenith angle between 177.50° and 178.25°) may result from inaccuracies in the DSM, as these pixels most likely view flat roofs in the RW.

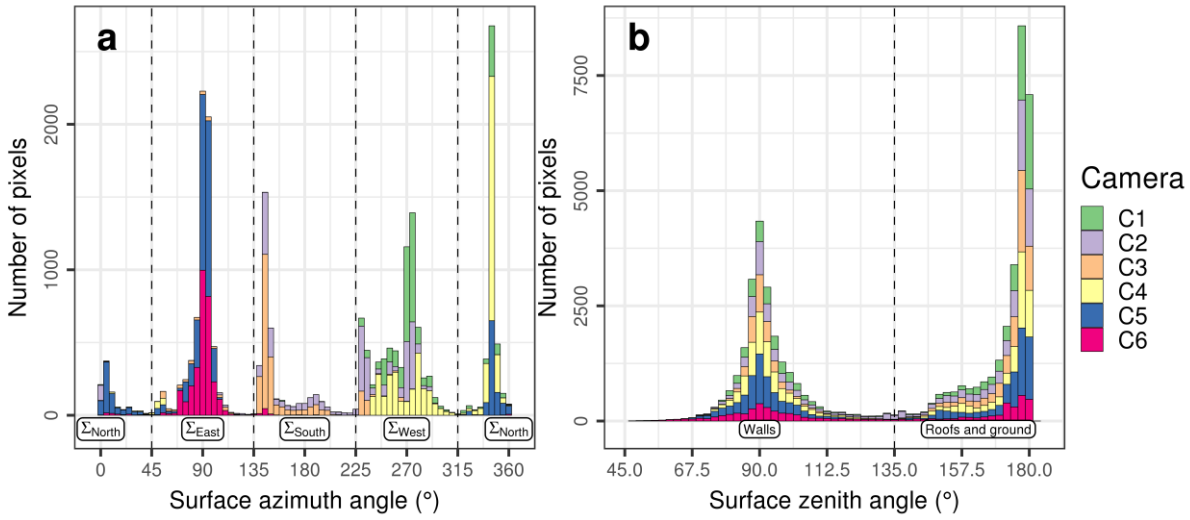

Fig 6. Frequency of pixels by surface orientations within the instantaneous field of view (IFOV) of each camera (excluding vegetation canopy elements (VCE) but including "mixed" and "masked" pixels) for (a) azimuth facing (zenith angle <135°), and (b) zenith angles of pixels. Azimuth angle of 0° (180°) is north (south) for WGS84 UTM grid zone 31N. Pixels with a zenith angle of 90° (180°) face vertically (horizontally).

4. Surface temperature variability by class

To quantify the role of surface class on T_s variability, the permutations of surface class in the observations (Table 3) are considered by scale:

1) building scale variability (facet, orientation, and material Σ, e.g. Fig 2b),

2) sub-facet variability within a surface orientation (e.g. different roof slopes) related to the sun-surface geometry ($\overline{BRF}$, e.g. Fig 2c), and

3) shadow history with high spatial resolution ($t_{shd,}$ e.g. Fig 2d).

4.1 Variability from surface orientation and material at the building scale

Across all pre-classified observations (Fig 7a, white) the overall T_s difference is 37.5 K between the 5th percentile (P_5) and P_{95} during the period 12:00 – 12:55 (hereafter referred to by time ending, i.e. 13:00). Mixed pixels (Fig 7a, grey), primarily walls with complex small-scale features (e.g. balconies - C6, Fig 2a, b), are generally cooler than roof and ground surfaces, with a smaller hourly and diurnal range than the pre-classified temperatures. Hilland and Voogt (2020) resolve these small-scale features and find self-shading significantly reduces facet averaged T_s by around 1 - 6 K.

With our coarsest surface classification (i.e. building facets, orientations and materials) roof T_s, as expected (Voogt and Grimmond, 2000; Christen *et al.*, 2012; Adderley *et al.*, 2015), has the greatest diurnal T_s range (Fig 7b, median $\Sigma_{roof[dark]}$ 290.6 → 329.0 K). T_s across $\Sigma_{roof[dark]}$ pixels consistently

shows most variation at all times. Driven by insolation, intra-facet T_s variability for $\Sigma_{roof[dark]}$ is between 302.1 and 336.3 K (P_5 and P_{95}) at 12:00, with P_{95} - P_5 differences consistently over 20 K between 10:00 and 16:00. The higher albedo of $\Sigma_{roof[light]}$ surfaces means less shortwave radiation is absorbed which leads to lower T_s with median $\Sigma_{roof[light]}$ (313.8 K) at 13:00 being 14.2 K lower than the coinciding $\Sigma_{roof[dark]}$ temperature (Fig 7b). Prior to an overcast period in the afternoon (15:30 – 15:55) the two roof types have distinct T_s distributions. The fewer $\Sigma_{roof[light]}$ pixels are mainly sunlit throughout the day, whereas $\Sigma_{roof[dark]}$ areas have some within-canopy surfaces affected by prolonged (> 1 h) shadowing. Overcast conditions cause the distributions to slightly converge as the contrasting albedos have reduced effect when only diffuse incident solar radiation is incident. The subsequent lower sun angles reduce the overall shortwave radiative forcing.

Grass ($\Sigma_{Ground[grass]}$) T_s has a smaller diurnal range than impervious ground ($\Sigma_{Ground[imp.]}$). Grass temperatures are affected by both evaporative cooling and shadowing from grass blades (i.e. leaf area index is greater than 1) whereas the impervious areas lack moisture (4 days since rainfall). Also, the generally higher heat capacities of $\Sigma_{Ground[imp.]}$ cause more heat to be stored during the day and released slowly over night. Uncertainty in grass T_s may arise from a potential sample bias as only one camera (C1) views this surface class whereas all cameras see some $\Sigma_{Ground[imp.]}$. The relatively coarse (4 m) land cover dataset (Lindberg and Grimmond, 2011) may introduce unquantified classification uncertainties.

Considering wall pixels by cardinal orientation, Σ_{East} (Σ_{West}) pixels are warmest during morning (afternoon), with median T_s reaching 306.1 (310.6) K at 11:00 (17:00). Σ_{West} surfaces peak at higher temperatures than Σ_{East}, as the latter are among the first to be heated in the morning while Σ_{West} surfaces have already been heated throughout the day. Σ_{West} remains warm past sunset (sunset at ~18:55 UTC) and is 1.2 K warmer than Σ_{North} at 23:00 (differences in per-pixel median). This is reasonable given Σ_{North} pixels are mainly shaded throughout the day so that their T_s is consistently low with less variability. Shortly prior to sunset, Σ_{North} surfaces receive a little direct solar irradiation which causes their T_s to be slightly greater than that of Σ_{East} pixels in the evening. The T_s medians across wall orientations consistently differ by over 10 K between 10:00 and 15:00 (maximum difference is 18.1 K at 12:00).

The sampling bias of south-east walls (Section 3) causes the median T_s for Σ_{South} to peak (315.8 K) at 12:00, i.e. earlier than would be expected for a wall distribution centred around 180° azimuth. Before sunrise, median T_s differences between wall orientations are less than 0.8 K but are up to 4.9 K warmer than $\Sigma_{Roof[dark]}$ at 01:00 during a clear-sky nocturnal period (consistent with e.g. Lagouarde *et al.*, 2004). During daytime, walls are generally much cooler than roofs. Their complex geometry and material compositions contribute to wall T_s variability. The study area roofs are mostly planar with small features (e.g. chimneys and air conditioning units) whereas walls have many balconies and

other shade-causing features that reduce their overall temperature. As glass emissivity is unaccounted for, wall T_s may be overestimated (Morrison *et al.*, 2020). Glass and windows ("Σ_{Glass}") were not classified as the resolution of data used to construct the DSM (Google Earth images, Morrison *et al.*, 2020) is too coarse. No buildings in the study area have fully glazed walls and glass windows are assumed to be evenly sampled across all cameras.

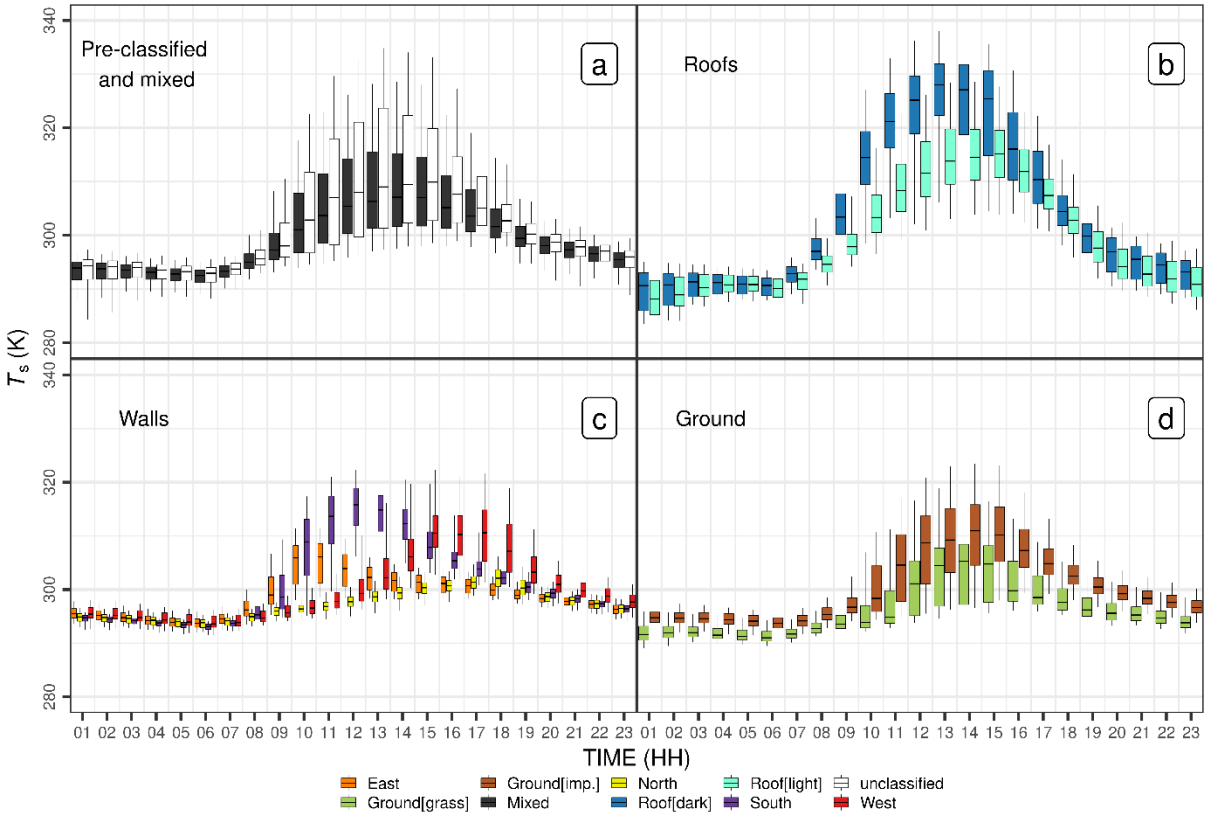

Fig 7. Variability of LWIR camera derived surface temperature (T_s) for 27th August with observations classified as (a) unclassified (white) (except vegetation canopy elements and "masked" and "mixed" (grey) pixels), (b) roofs, (c) walls, and (d) ground. Boxplots use data from all camera images (5 min samples) by group (colour) during 1 h (e.g. first hour is 00:00 → 00:55 for Time (HH) "01" between vertical lines) with interquartile range (box), median (horizontal line) and 5 and 95 percentiles (whiskers) of pixel values.

4.2 Variability from shortwave irradiance

T_s by facet (orientation and material) have positive correlation with irradiance using sun-surface geometry (bidirectional reflectance factor, $\overline{BRF}$) (cf. Fig 2a, c). To assess the importance of BRF as a driver for T_s of the low albedo roofs ($\Sigma_{Roof[dark]}$), the difference between sunlit flat [$T_s(BRF \approx 1)$] and all other binned sun-surface geometry configurations [$T_s(\overline{BRF})$] for roofs (Fig 8) is calculated through a day. Overall, there is clear separation in T_s between $\overline{BRF}$ bins. At 09:15, median T_s differences between sloped and flat sunlit roofs reach 13.2 K [$T_s(\overline{BRF} = 1.5)$ - $T_s(BRF \approx 1)$, Fig 8]. Sloped roofs with $\overline{BRF} < 1$ but still sunlit have median T_s up to 23.3 K cooler than the flat roofs at 11:55. Contributions to the observed T_s variability within each $\overline{BRF}$ bin at a given timestep are linked to the variable time in sun (Fig 2d), differences in surface albedo and emissivity within the $\Sigma_{Roof[dark]}$ surface property, and uncertainties in atmosphere and emissivity corrections (Morrison *et al.*, 2020).

During the overcast period (15:30 – 15:55) when $\overline{BRF}$ = -1 for all surfaces, there are smaller differences in $T_s(\overline{BRF})$ which persists into the evening (Fig 8). A subset of all possible roof slope angles are sampled, meaning some arrangements of sun-surface angles (and therefore $\overline{BRF}$) are not observed for sloped roofs. This results in gaps of $T_s(\overline{BRF})$ at times (e.g. $T_s(\overline{BRF} = 0.25)$ for around 12:00 → 14:00). Large gaps (> 4 h) for high BRF bins ($\overline{BRF}$ > 1.25) occur with high sun angles (i.e. peaks in $E_\lambda^{\downarrow,dir}$, Eqn. 1). During these gaps the near-flat roofs are irradiated most and $T_s(\overline{BRF} = 1.25)$ is the highest physically possible bin around midday (± ~ 2.5 h) for the study site latitude and corresponding solar elevation maximum.

Applied to vertical facets (Supplementary material 1), this sun-surface geometry analysis shows most T_s variation is captured by wall orientation (Fig 7c). For ground surfaces, most observations are of flat ground (i.e. BRF ≈ 1).

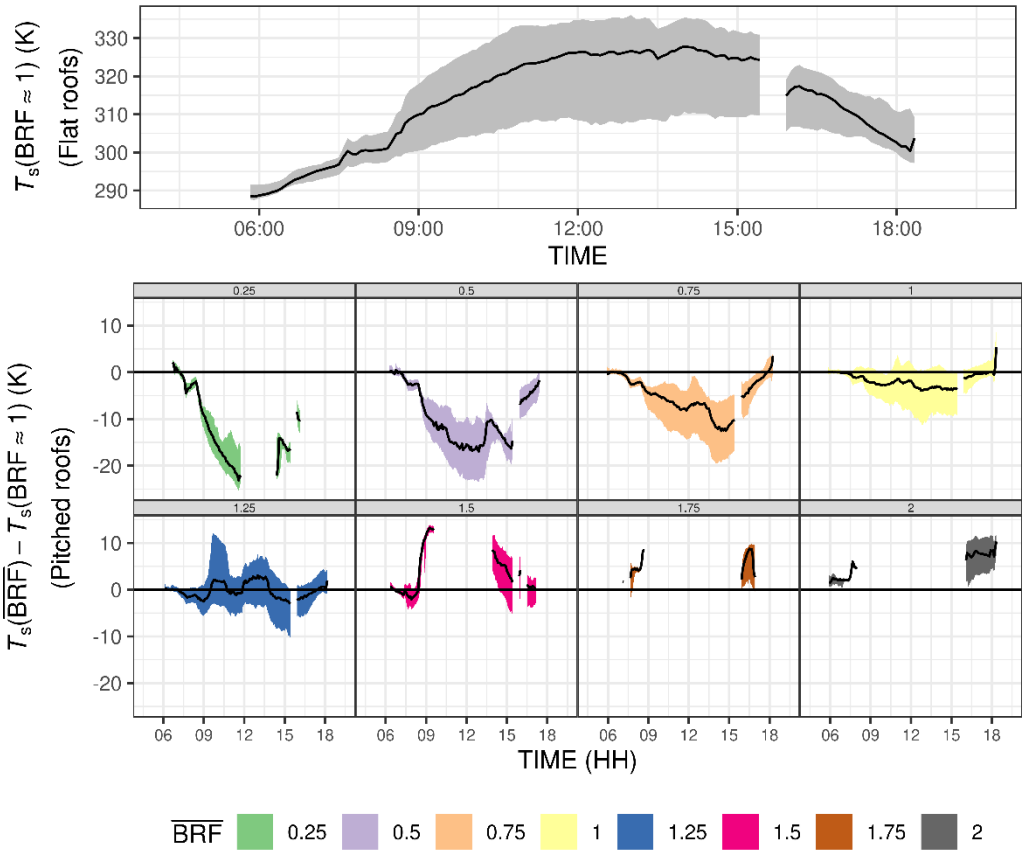

Fig 8. Observed daytime roof surface temperature (T_s) for 27th August for pixels classified with bidirectional reflectance factor (BRF, Schaepman-Strub *et al.*, 2006) (top) equivalent to solar irradiance for a flat surface (BRF ≈ 1) and (bottom) by $\overline{BRF}$ (bin width 0.25) as difference from BRF ≈ 1 (i.e. across all observed sun-surface geometries). DART calculated BRF assuming Lambertian surfaces.

4.3 Variability from shadow history

Shadow history has a potentially significant impact on T_s variability given the large and variable thermal inertia of urban materials (e.g. concrete, Arnfield and Grimmond, 1998). We explore the micro-scale persistence effects of shadows on upwelling longwave radiation with thermography

(Meier *et al.*, 2010) with multiple cameras and objectively determined shadow distributions across the images.

For the study day, 1.15 x 10^6 per-pixel cooling events [$\tau(x, y, t, \Sigma)$] are identified from all cameras (Fig 9). The model fits for each cooling event (Section 2.3) have mean absolute error (MAE) of 0.7 K (ground, roof) or 0.6 K (walls) and are linear (red dashed line, Fig 9 row 1) across the range of T_s differences (approx. 0 → 30 K). A small number of points have negative differences, indicating the shaded ambient T_s is warmer than the recently shaded T_s. Through manual inspection, negative differences for roofs pixels are associated with microscale features in the foreground roof of C6 (approx. centre of image, Fig 2a). These roof features may have low emissivity materials or complex geometry unresolved by the DSM. Negative differences for walls are explained by C2's $\Sigma_{West}(x, y)$ pixels near the building with $\Sigma_{Roof[light]}$ (Fig 2b). This concrete wall extents above the canyon height so that the relatively high sky view factor and direct solar illumination until sunset are likely causing recently shaded T_s to be lower temperature than the ambient reference. The latter is more representative of warmer inside-canyon walls. Overall, these departures from exponential cooling give the flat "tail" to the scatter (e.g. Fig. 9, wall, row 1), as negative modelled values are not permitted. Negative differences account for 1.3 % of all cooling events (sunlit - shaded difference of -2.5 K at P_5).

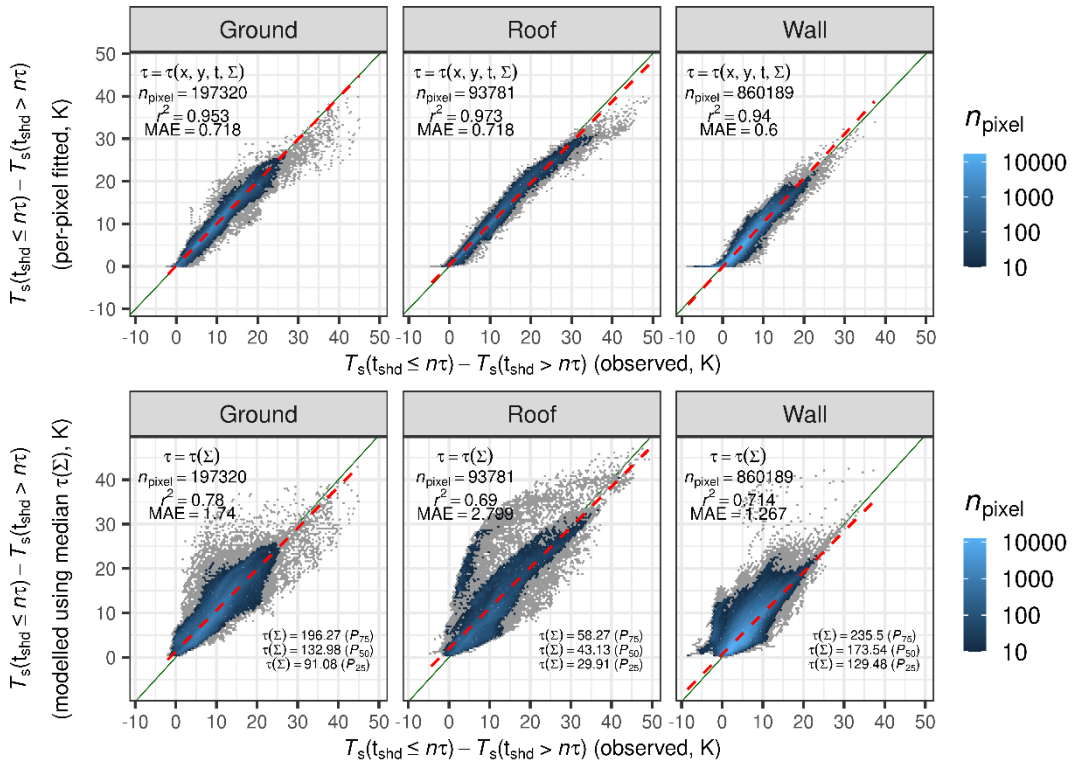

Fig 9. Surface temperature (T_s) cooling rates observed (x axis) and estimated (using Eqn. 3) for each pixel with pixels numbers (n_{pixel}) indicated (colours) with (row 1) fitted time constant τ per pixel [τ(x, y, Σ)] and (row 2) modelled time constant as median τ(x, y, t, Σ) per surface type [τ(Σ)] for (column 1) ground (grass and impervious), (column 2) roof (light and dark) and (column 3) walls (N, E, S, W). Statistics: coefficient of determination (r^2), mean absolute error (MAE, K).

The generalised values of τ [τ(Σ)] (Fig 9 row 2 labels), determined from the median of τ(x, y, t, Σ) pixels (Section 2.3), allow inter-facet T_s cooling rates to be compared. Roofs generally cool much faster ($\tau(\Sigma_{Roof})$ = 43.13 min) than ground ($\tau(\Sigma_{Ground})$ = 132.98 min) and walls, which cool around four times slower ($\tau(\Sigma_{Walls})$ = 173.54 min). As τ(x, y, t, Σ) is highly variable (e.g. $\tau(\Sigma_{Ground})$ is 91.08 → 196.27 min for P_{25} → P_{75}), using these generalised median values of τ(x, y, t, Σ) results in a greater spread between observed and modelled results (Fig 9 cf. row 1 and 2). There is generally good agreement between observed cooling rates and the generalised modelled results (Fig 9 row 2) but with some large (> 10 K) departures when facets have distinctly different thermal properties. Uncertainty is increased for roofs as their shading during daytime can only be from micro-scale roof geometry or from nearby taller buildings (e.g. Fig 2b, foreground of C2 and C3) which is mostly confined to short periods. This reduces the number of pixels available for the ambient T_s estimation (Section 2.3). Additionally, the emissivity correction uncertainty is greatest for roof surfaces because of the large contrast between LWIR irradiance (from the relatively cool sky) and LWIR exitance (Morrison *et al.*, 2020).

Instances of poor model agreement for ground pixels may arise from the highly contrasting material properties (impervious and grass), whereas for walls the more complex surface geometry may lead to uncertainties in shadow patterns and history. Walls also have a mix of glass and masonry/concrete with their contrasting thermal properties and cooling rates not accounted for.

The cooling rate model and the spread in Fig 9 (row 2) are summarised (Table 5) using a subset of observations (P_{95} differences between recently shaded and ambient after 10 minutes in shade, to represent surfaces that have been heated by the sun throughout the day) modelled at various times in shade using $\tau(\Sigma)$ values. After 10 min, these recently shaded roofs differ most to the ambient temperature (27.5 K warmer than ambient). They exponentially cool the fastest (2.1 K warmer than ambient after 90 min using $\tau(\Sigma_{Roof})$ P_{50}, 0.7 K → 4.1 K across interquartile range - IQR) as $\tau(\Sigma_{Roof})$ is lower than $\tau(\Sigma_{Wall})$ and $\tau(\Sigma_{Ground})$. The higher $\tau(\Sigma)$ for walls and ground means there are still significant differences to the ambient temperature after long periods of cooling. After 90 min the walls are 8.8 K (7.1 K → 10.3 K IQR) warmer than ambient.

Table 5. Differences in surface temperature (T_s) between recently shaded surfaces (i.e. short t_{shd} - time in shade) and a reference ambient $T_s(t_{shd} > n\tau)$ for 95th percentile (P_{95}) of observed thermal camera measurements in central London (27th August 2017) modelled (Section 2.3) at t_{shd} of 30, 60 and 90 min using observationally derived cooling time constants (τ) for each surface type. E.g. where recently shaded ground is 21.6 K warmer than ambient after t_{shd} = 10 min, this difference exponentially reduces to 18.6 K after 30 min (17.3 K → 19.5 K interquartile range using 196.27 min → 91.08 min time constants) using time constant $\tau(\Sigma)$ = 132.98 (Fig 9 row 2 "Ground" label) and assuming no change in ambient temperature. See Fig 9 for all $\tau(\Sigma)$ percentiles and Eqn. 3 for exponential cooling model.

Recently shaded - ambient $T_s(t_{shd} \leq n\tau)$ - $T_s(t_{shd} > n\tau)$ **(K)**	**Time in shade (t_{shd})**									
	10 min	30 min			60 min			90 min		
	observed	P_{25}	P_{50}	P_{75}	P_{25}	P_{50}	P_{75}	P_{25}	P_{50}	P_{75}
Ground	21.6	17.3	18.6	19.5	12.5	14.8	16.7	6.5	9.4	12.3
Roof	27.5	14.1	17.3	19.5	5.2	8.6	11.7	0.7	2.1	4.1
Walls	16.5	14.1	14.7	15.2	11.2	12.4	13.3	7.1	8.8	10.3

Previous observations acknowledge that shaded surface temperatures exhibit variation from shadow histories (Voogt, 2008; Morrison *et al.*, 2018), but often aggregate the shaded temperatures to a single value. This work demonstrates the possibility to stratify shaded temperatures instead by shadow history using a simple exponential rate of cooling. Variability in τ is directly related to variability in heat transfer rate (radiative, convective, and conductive), material heat capacities, density, volume, and overall mass of the observed surface structures. For example, rapid cooling rate of roofs (median cooling time constants $\tau(\Sigma_{Roof})$ = 43.13 min) may be explained by a lower mass (cf. walls, Xu and Asawa, 2020) facilitating conductive heat loss, higher sky view factor (facilitating radiative heat transfer), and exposure to higher wind speeds (facilitating convective heat transfer).

5. Conclusions

Analysis of a fusion of observation (ground-based thermography) and modelling (urban geometry, material properties, sensor views and radiative transfer processes) data on a mainly clear-sky summer day in central London are used to explore various drivers of surface temperature (T_s) variability. With a very high level of detail surface description and integrated sensor view modelling, the camera source area analysis is unprecedented for such a complex (i.e. realistic) urban setting. General and study specific conclusions about the observation process are:

- Cameras installed on higher buildings have a better vantage and larger source area.

- In this study, the source area is 15.6 % roofs, 41.6 % walls (~10 % per cardinal direction) and 22.6 % ground (remainder above ground vegetation).
- Even with six cameras the source area is only 9.5 % of the overall area (430 m x 430 m horizontal extent).
- All pixels are assumed to sample equal portions of the surface yet in reality the surface area covered by a pixel varies across the image due to viewing geometry. Future work should investigate methods to weight aggregated observations by per-pixel source area.

Objective image classification separates drivers of T_s variability without requiring manual image classification or statistical inference.

- Observed T_s is highly variable.
  - In this study the 5^{th} - 95^{th} percentile differences in per-pixel T_s observations reach up to 37.5 K during daytime.
  - Diurnal patterns of T_s for surfaces with different orientation show general agreement with prior studies at similar latitude.

Highly detailed image classification enables T_s variability to be quantified in direct relation to the sun-surface geometry features, including the amount of short- and long-wave radiation incident onto a surface, driving shadow patterns, direct solar irradiance and radiation trapping between buildings.

- Material properties are especially important for roof surfaces with increased access to solar radiation and high exposure to the cold sky. This effect is expected to be particularly important for thermal spaceborne earth observation, where near-nadir remote sensing observations have a view bias of horizontal facets.
- Variability of T_s is driven by surface orientation to the sun of the facet (e.g. walls, roofs, ground) and sub-facet characteristics (e.g. flat or sloped roofs, high or low albedo roofs).
- Variation in surface temperature across a single facet can be of similar magnitude to the variation between the median temperatures of different facet types.
  - Across all roof pixels within a given hour (i.e. intra-roof) 5th - 95th percentile T_s differences are consistently over 20 K between 10:00 and 16:00 (max 34.2 K between 11:00 and 11:55)
  - Intra-roof variation is driven by sun-surface geometry effects. T_s differences between flat and sloped roofs reach 23.3 K around midday.
  - Pixel-level temperatures of walls stratified by cardinal direction and aggregated to median values (i.e. inter-wall) differ by up to 18.1 K between north (median 297.7 K) and south (median 315.8 K) facets around midday. Including roof and ground faceT_s,

median differences reach 29.3 K at 13:00 between the low albedo roof (median 328.0 K) and north facing wall (median 298.7 K).

The second important driver of T_s variability are shadows. For the first time, the effect of shadows through time on T_s is quantified across a real convoluted urban surface.

- The history of surface shadows greatly affects T_s. Recently shaded roof surfaces are up to 27.5 K warmer than those in shade for long periods.
- Cooling characteristics were modelled from observations using exponential functions with time constants (τ) estimated relative to long-term shaded surface temperatures. Clear contrasts were found between facet types: roofs on average cool much faster $\tau(\Sigma_{\mathrm{Roof}}) = 43.13$ min than ground $\tau(\Sigma_{\mathrm{Ground}}) = 132.98$ min and walls $\tau(\Sigma_{\mathrm{Walls}}) = 173.54$ min.
- Surfaces shaded at sunset will have cooled to within 5 % of the ambient temperature by ~3τ i.e. over 6 h and 8.5 h into the night for ground and walls, respectively.
- This shadow history methodology could be extended to study recently sunlit temperatures.

Material properties determine the amount of incoming energy absorbed.

- Using simple albedo characteristics (i.e. two classes “light” (high albedo) and “dark” (low albedo); excluding any metal or glass) clearly separates observed temperature distributions.
    - Dark roofs are up to 14.2 K warmer during the day as more solar radiation is absorbed.
- Material classification would benefit from more detailed data (e.g. surface optical material properties), particularly for glass and windows which can directionally scatter longwave radiation (e.g. specular reflections) and confound the T_s retrieval (Morrison *et al.*, 2020). Further classification requires more detailed visible imagery from e.g. Google Street view, (Li *et al.*, 2018; Gong *et al.*, 2018), study-specific vehicle traverses (Hilland and Voogt, 2020) or manual inspection (Christen *et al.*, 2012).

Overall, the combination of a relatively large fraction of vegetation, complex geometry and associated T_s distributions give a unique temporally continuous dataset. Observations and the underlying methods for their retrieval and classification could be used as input and to evaluate unstably stratified large eddy simulation modelling (Gronemeier *et al.*, 2017) and building energy balance models (Bueno *et al.*, 2012), or input to radiative transfer models such as DART (Gastellu-Etchegorry *et al.*, 2015) for evaluation of effective thermal anisotropy (Krayenhoff and Voogt, 2016; Morrison *et al.*, 2018; Wang *et al.*, 2018).

These data provide useful insights for meso-scale weather and larger scale climate models which simplify the urban surface to facets (Masson, 2000; Harshan *et al.*, 2018) assuming flat roofs with a uniform height (Harman *et al.*, 2004; Krayenhoff and Voogt, 2007). Both the extent of intra-facet surface temperature variability and the net surface cooling rate variability provide some insights into

the processes that are "averaged" into composite values. Through ensemble modelling, the implications of this variability on averaged flux calculations and therefore weather/climate predictions should be assessed. For many of the larger spatial and temporal extent applications, further observations should assess how representative our study results are with respect to time of year and location (across London, other cities).

Acknowledgements

This work is funded by Newton Fund/Met Office Climate Science for Service Partnership China (SG), EPSRC DARE (EP/P002331/1), H2020 UrbanFluxes (637519), Met Office Joint Chair and ERC urbisphere 855005. We thank Islington Council (Esther Lamontagne and Paul Stokes) for arranging access to observation sites and Kjell Zum Berge (University of Reading) for assistance with the observations.

References

Acuña Paz y Miño, J., Lawrence, C. and Beckers, B. (2020) 'Visual metering of the urban radiative environment through 4π imagery', *Infrared Physics & Technology*, 110, p. 103463. doi: 10.1016/j.infrared.2020.103463.

Adderley, C., Christen, A. and Voogt, J. A. (2015) 'The effect of radiometer placement and view on inferred directional and hemispheric radiometric temperatures of an urban canopy', *Atmospheric Measurement Techniques*, 8(7), pp. 2699–2714. doi: 10.5194/amt-8-2699-2015.

Alchapar, N. L., Correa, E. N. and Cantón, M. A. (2014) 'Classification of building materials used in the urban envelopes according to their capacity for mitigation of the urban heat island in semiarid zones', *Energy and Buildings*, 69, pp. 22–32. doi: 10.1016/j.enbuild.2013.10.012.

Alexander, P. J., Fealy, R. and Mills, G. (2015) 'Spatial validation of an urban energy balance model using multi-temporal remotely sensed surface temperature', in *2015 Joint Urban Remote Sensing Event (JURSE)*. IEEE, pp. 1–4. doi: 10.1109/JURSE.2015.7120500.

Antoniou, N., Montazeri, H., Neophytou, M. and Blocken, B. (2019) 'CFD simulation of urban microclimate: Validation using high-resolution field measurements', *Science of The Total Environment*, 695, p. 133743. doi: 10.1016/j.scitotenv.2019.133743.

Arnfield, A. J. and Grimmond, C. S. B. (1998) 'An urban canyon energy budget model and its application to urban storage heat flux modeling', *Energy and Buildings*, 27(1), pp. 61–68. doi: 10.1016/s0378-7788(97)00026-1.

Asano, K. and Hoyano, A. (1998) 'Application of a new spherical thermography technique to monitoring of outdoor long-wave radiant fields', in Andresen, B. F. and Strojnik, M. (eds),

p. 317. doi: 10.1117/12.328081.

Bird, R. E. and Hulstrom, R. L. (1981) ‘Simplified clear sky model for direct and diffuse insolation on horizontal surfaces’. doi: 10.2172/6510849.

Blender (2018) ‘Blender 2.79b’. Blender Institute, Amsterdam.

Bueno, B., Pigeon, G., Norford, L. K., Zibouche, K. and Marchadier, C. (2012) ‘Development and evaluation of a building energy model integrated in the TEB scheme’, *Geoscientific Model Development*, 5(2), pp. 433–448. doi: 10.5194/gmd-5-433-2012.

Chen, F., Kusaka, H., Bornstein, R., Ching, J., Grimmond, C. S. B., *et al.* (2011) ‘The integrated WRF/urban modelling system: development, evaluation, and applications to urban environmental problems’, *International Journal of Climatology*, 31(2), pp. 273–288. doi: 10.1002/joc.2158.

Christen, A., Meier, F. and Scherer, D. (2012) ‘High-frequency fluctuations of surface temperatures in an urban environment’, *Theoretical and Applied Climatology*, 108(1–2), pp. 301–324. doi: 10.1007/s00704-011-0521-x.

Crawley, D. B., Lawrie, L. K., Winkelmann, F. C., Buhl, W. F., Huang, Y. J., *et al.* (2001) ‘EnergyPlus: creating a new-generation building energy simulation program’, *Energy and Buildings*, 33(4), pp. 319–331. doi: 10.1016/S0378-7788(00)00114-6.

Evans, S., Hudson-Smith, A. and Batty, M. (2011) ‘3-D GIS: Virtual London and beyond’, *Cybergeo*. doi: 10.4000/cybergeo.2871.

Fröhlich, D., Gangwisch, M. and Matzarakis, A. (2019) ‘Effect of radiation and wind on thermal comfort in urban environments - Application of the RayMan and SkyHelios model’, *Urban Climate*, 27, pp. 1–7. doi: 10.1016/j.uclim.2018.10.006.

Gaitani, N., Burud, I., Thiis, T. and Santamouris, M. (2017) ‘High-resolution spectral mapping of urban thermal properties with Unmanned Aerial Vehicles’, *Building and Environment*, 121, pp. 215–224. doi: 10.1016/j.buildenv.2017.05.027.

Gastellu-Etchegorry, J. P., Yin, T., Lauret, N., Cajgfinger, T., Gregoire, T., *et al.* (2015) ‘Discrete anisotropic radiative transfer (DART 5) for modeling airborne and satellite spectroradiometer and LIDAR acquisitions of natural and urban landscapes’, *Remote Sensing*, 7(2), pp. 1667–1701. doi: 10.3390/rs70201667.

Gastellu-Etchegorry, J. P., Grau, E. and Lauret, N. (2012) ‘DART: A 3D Model for Remote Sensing Images and Radiative Budget of Earth Surfaces’, in *Modeling and Simulation in Engineering*. InTech. doi: 10.5772/31315.

588 Gong, F. Y., Zeng, Z. C., Zhang, F., Li, X., Ng, E., *et al.* (2018) 'Mapping sky, tree, and building
589 view factors of street canyons in a high-density urban environment', *Building and*
590 *Environment*, 134(February), pp. 155–167. doi: 10.1016/j.buildenv.2018.02.042.

591 Google (2019) 'Google Earth Pro', *Google*. Google.

592 Gronemeier, T., Raasch, S. and Ng, E. (2017) 'Effects of unstable stratification on ventilation in
593 Hong Kong', *Atmosphere*, 8(9), pp. 1–15. doi: 10.3390/atmos8090168.

594 Harman, I. N., Best, M. J. and Belcher, S. E. (2004) 'Radiative exchange in an urban street canyon',
595 *Boundary-Layer Meteorology*, 110(2), pp. 301–316. doi: 10.1023/A:1026029822517.

596 Harshan, S., Roth, M., Velasco, E. and Demuzere, M. (2018) 'Evaluation of an urban land surface
597 scheme over a tropical suburban neighborhood', *Theoretical and Applied Climatology*,
598 133(3–4), pp. 867–886. doi: 10.1007/s00704-017-2221-7.

599 Hartley, R. ~I. and Zisserman, A. (2004) *Multiple View Geometry in Computer Vision*. Second.
600 Cambridge University Press, ISBN: 0521540518.

601 Hartz, D. A., Prashad, L., Hedquist, B. C., Golden, J. and Brazel, A. J. (2006) 'Linking satellite
602 images and hand-held infrared thermography to observed neighborhood climate conditions',
603 *Remote Sensing of Environment*, 104(2), pp. 190–200. doi: 10.1016/j.rse.2005.12.019.

604 Hénon, A., Mestayer, P. G., Lagouarde, J. P. and Voogt, J. A. (2012) 'An urban neighborhood
605 temperature and energy study from the CAPITOUL experiment with the Solene model: Part
606 2: Influence of building surface heterogeneities', *Theoretical and Applied Climatology*,
607 110(1–2), pp. 197–208. doi: 10.1007/s00704-012-0616-z.

608 Hilland, R. V. J. and Voogt, J. A. (2020) 'The effect of sub-facet scale surface structure on wall
609 brightness temperatures at multiple scales', *Theoretical and Applied Climatology*, 140(1–2),
610 pp. 767–785. doi: 10.1007/s00704-020-03094-7.

611 Hu, L. and Wendel, J. (2019) 'Analysis of urban surface morphologic effects on diurnal thermal
612 directional anisotropy', *ISPRS Journal of Photogrammetry and Remote Sensing*,
613 148(December 2018), pp. 1–12. doi: 10.1016/j.isprsjprs.2018.12.004.

614 Kanda, M., Kawai, T., Kanega, M., Moriwaki, R., Narita, K., *et al.* (2005) 'A simple energy balance
615 model for regular building arrays', *Boundary-Layer Meteorology*, 116(3), pp. 423–443. doi:
616 10.1007/s10546-004-7956-x.

617 Krayenhoff, E. S., Jiang, T., Christen, A., Martilli, A., Oke, T. R., *et al.* (2020) 'A multi-layer urban
618 canopy meteorological model with trees (BEP-Tree): Street tree impacts on pedestrian-level
619 climate', *Urban Climate*, 32(July 2019), p. 100590. doi: 10.1016/j.uclim.2020.100590.

620 Krayenhoff, E. and Voogt, J. (2016) 'Daytime Thermal Anisotropy of Urban Neighbourhoods:
621 Morphological Causation', *Remote Sensing*, 8(2), p. 108. doi: 10.3390/rs8020108.

622 Krayenhoff, S. E. and Voogt, J. A. (2007) 'A microscale three-dimensional urban energy balance
623 model for studying surface temperatures', *Boundary-Layer Meteorology*, 123(3), pp. 433–
624 461. doi: 10.1007/s10546-006-9153-6.

625 Kusaka, H. and Kimura, F. (2004) 'Coupling a single-layer urban canopy model with a simple
626 atmospheric model: Impact on urban heat island simulation for an idealized case', *Journal of*
627 *the Meteorological Society of Japan*, 82(1), pp. 67–80. doi: 10.2151/jmsj.82.67.

628 Lagouarde, J. P., Moreau, P., Irvine, M., Bonnefond, J. M., Voogt, J. A., *et al.* (2004) 'Airborne
629 experimental measurements of the angular variations in surface temperature over urban
630 areas: Case study of Marseille (France)', *Remote Sensing of Environment*, 93(4), pp. 443–
631 462. doi: 10.1016/j.rse.2003.12.011.

632 Lee, S., Moon, H., Choi, Y. and Yoon, D. K. (2018) 'Analyzing thermal characteristics of urban
633 streets using a thermal imaging camera: A case study on commercial streets in Seoul,
634 Korea', *Sustainability (Switzerland)*, 10(2), pp. 1–21. doi: 10.3390/su10020519.

635 Li, X., Ratti, C. and Seiferling, I. (2018) 'Quantifying the shade provision of street trees in urban
636 landscape: A case study in Boston, USA, using Google Street View', *Landscape and Urban*
637 *Planning*, 169(August 2017), pp. 81–91. doi: 10.1016/j.landurbplan.2017.08.011.

638 Lindberg, F. and Grimmond, C. S. B. (2011) 'The influence of vegetation and building morphology
639 on shadow patterns and mean radiant temperatures in urban areas: model development and
640 evaluation', *Theoretical and Applied Climatology*, 105(3–4), pp. 311–323. doi:
641 10.1007/s00704-010-0382-8.

642 Masson, V. (2000) 'A physically-based scheme for the urban energy budget in atmospheric models',
643 *Boundary-Layer Meteorology*, 94(3), pp. 357–397. doi: 10.1023/A:1002463829265.

644 Meier, F., Scherer, D., Richters, J. and Christen, A. (2011) 'Atmospheric correction of thermal-
645 infrared imagery of the 3-D urban environment acquired in oblique viewing geometry',
646 *Atmospheric Measurement Techniques*, 4(5), pp. 909–922. doi: 10.5194/amt-4-909-2011.

647 Meier, F., Scherer, D. and Richters, J. (2010) 'Determination of persistence effects in spatio-
648 temporal patterns of upward long-wave radiation flux density from an urban courtyard by
649 means of Time-Sequential Thermography', *Remote Sensing of Environment*, 114(1), pp. 21–
650 34. doi: 10.1016/j.rse.2009.08.002.

651 Morrison, W., Kotthaus, S., Grimmond, C. S. B., Inagaki, A., Yin, T., *et al.* (2018) 'A novel method

652 to obtain three-dimensional urban surface temperature from ground-based thermography',
653 *Remote Sensing of Environment*, 215(December 2017), pp. 268–283. doi:
654 10.1016/j.rse.2018.05.004.

655 Morrison, W., Yin, T., Lauret, N., Guilleux, J., Kotthaus, S., *et al.* (2020) 'Atmospheric and
656 emissivity corrections for ground-based thermography using 3D radiative transfer
657 modelling', *Remote Sensing of Environment*, 237(December 2019), p. 111524. doi:
658 10.1016/j.rse.2019.111524.

659 Naughton, J. and McDonald, W. (2019) 'Evaluating the Variability of Urban Land Surface
660 Temperatures Using Drone Observations', *Remote Sensing*, 11(14), p. 1722. doi:
661 10.3390/rs11141722.

662 Offerle, B., Grimmond, C. S. B., Fortuniak, K. and Pawlak, W. (2006) 'Intraurban differences of
663 surface energy fluxes in a central European City', *Journal of Applied Meteorology and*
664 *Climatology*, 45(1), pp. 125–136. doi: 10.1175/JAM2319.1.

665 Optris GmbH (2018) 'Optris PI Operator's Manual'. Germany.

666 Pearlmutter, D., Berliner, P. and Shaviv, E. (2006) 'u', *Building and Environment*, 41(6), pp. 783–
667 795. doi: 10.1016/j.buildenv.2005.03.017.

668 Perpiñán, O. (2012) '{solaR}: Solar Radiation and Photovoltaic Systems with {R}', *Journal of*
669 *Statistical Software*, 50(9), pp. 1–32. Available at: http://www.jstatsoft.org/v50/i09/.

670 Porson, A., Clark, P. A., Harman, I. N., Best, M. J. and Belcher, S. E. (2010) 'Implementation of a
671 new urban energy budget scheme in the MetUM. Part I: Description and idealized
672 simulations', *Quarterly Journal of the Royal Meteorological Society*, 136(651), pp. 1514–
673 1529. doi: 10.1002/qj.668.

674 Rotach, M. W., Vogt, R., Bernhofer, C., Batchvarova, E., Christen, A., *et al.* (2005) 'BUBBLE - An
675 urban boundary layer meteorology project', *Theoretical and Applied Climatology*, 81(3–4),
676 pp. 231–261. doi: 10.1007/s00704-004-0117-9.

677 Schaepman-Strub, G., Schaepman, M. E., Painter, T. H., Dangel, S. and Martonchik, J. V. (2006)
678 'Reflectance quantities in optical remote sensing-definitions and case studies', *Remote*
679 *Sensing of Environment*, 103(1), pp. 27–42. doi: 10.1016/j.rse.2006.03.002.

680 Toparlar, Y., Blocken, B., Vos, P., van Heijst, G. J. F., Janssen, W. D., *et al.* (2015) 'CFD simulation
681 and validation of urban microclimate: A case study for Bergpolder Zuid, Rotterdam',
682 *Building and Environment*, 83, pp. 79–90. doi: 10.1016/j.buildenv.2014.08.004.

683 Toparlar, Y., Blocken, B., Maiheu, B. and van Heijst, G. J. F. (2017) 'A review on the CFD analysis

of urban microclimate', *Renewable and Sustainable Energy Reviews*, 80, pp. 1613–1640. doi: 10.1016/j.rser.2017.05.248.

Vollmer, M. (2009) 'Newton's law of cooling revisited', *European Journal of Physics*, 30(5), pp. 1063–1084. doi: 10.1088/0143-0807/30/5/014.

Vollmer, M. and Möllmann, K.-P. (2017) *Infrared Thermal Imaging*. Weinheim, Germany: Wiley-VCH Verlag GmbH & Co. KGaA. doi: 10.1002/9783527693306.

Voogt, J. A. (2008) 'Assessment of an Urban Sensor View Model for thermal anisotropy', *Remote Sensing of Environment*, 112(2), pp. 482–495. doi: 10.1016/j.rse.2007.05.013.

Voogt, J. A. and Grimmond, C. S. B. (2000) 'Modeling surface sensible heat flux using surface radiative temperatures in a simple urban area', *Journal of Applied Meteorology*, 39(10), pp. 1679–1699. doi: 10.1175/1520-0450-39.10.1679.

Voogt, J. a. and Oke, T. R. (1997) 'Complete Urban Surface Temperatures', *Journal of Applied Meteorology*, 36(9), pp. 1117–1132. doi: 10.1175/1520-0450(1997)036<1117:CUST>2.0.CO;2.

Wang, D., Chen, Y. and Zhan, W. (2018) 'A geometric model to simulate thermal anisotropy over a sparse urban surface (GUTA-sparse)', *Remote Sensing of Environment*, 209(19), pp. 263–274. doi: 10.1016/j.rse.2018.02.051.

Xu, X. and Asawa, T. (2020) 'Systematic numerical study on the effect of thermal properties of building surface on its temperature and sensible heat flux', *Building and Environment*, 168(October 2019). doi: 10.1016/j.buildenv.2019.106485.